[1] **G. Divya**

[2] **Dr. Venkata Padmavathi S**

Intelligent Power Management of Electric vehicle with onboard PV by ANN-based Model Predictive Control

Abstract: - This paper presents a novel configuration of Hybrid Electric Vehicle (HEV) with fuel cell as primary source and an on-board Photovoltaic (PV) array as secondary source. It incorporates an advanced Model Predictive Control (MPC) system that utilizes Artificial Neural Network (ANN) technology to control induction motor of electric vehicle. The system has three main parts: a fuel cell, an electrolyzer, and a PV array. Each part has a different job in supplying power to the vehicle. The PV array functions to supplement the fuel cell by providing power when ample irradiation is available. When the car isn't being used, the extra power from the solar panels goes to the electrolyzer. There, it turns into chemical energy, making hydrogen. This hydrogen is stored in the onboard hydrogen tank for future use. To fulfil the voltage needs of both the motor and energy sources, a quadratic bidirectional buck-boost converter (QBBC) is utilized. This converter efficiently manages the voltage output while ensuring compatibility with various energy sources. The system undergoes comprehensive analysis under different irradiance and speed conditions to evaluate its performance and efficiency. To make the solar power system more efficient and cost-effective, a Maximum Power Point Tracking (MPPT) algorithm is used. This algorithm helps get the maximum power from the PV system. An improved incremental conductance algorithm is used for this, making sure it accurately finds the best power point. The control strategy incorporates both outer voltage and inner current control, to effectively control the DC output voltage of the QBBC. The vehicle's drive system employs an indirect vector-controlled induction motor. To regulate the motor's speed effectively, an advanced ANN-MPC system is used, providing precise control and high efficiency. This paper introduces a novel approach for predictive torque control of AC machines, eliminating the need for weighting factors. An ANN estimator is used to accurately expect the motor speed, which improves the overall performance of the control system. By using MATLAB/SIMULINK to test how well the proposed Electric Vehicle (EV) setup works and make sure it's effective in real-life situations. Through this comprehensive approach, the paper contributes to advancing the development of efficient and intelligent electric vehicle systems..

Keywords: Electric Vehicle (EV), Photovoltaic (PV) Array, Model Predictive Control (MPC), ANN, Quadratic Bidirectional Buck-Boost Converter, Indirect Vector-Controlled Induction Motor, Renewable Energy Integration.

I. INTRODUCTION

To help move towards a world without carbon emissions due to global warming, countries worldwide are increasing their efforts to boost the use of renewable energy sources, which can substitute fossil fuels [1]. The vehicle trade, which depends a lot on fossil fuels, is being closely looked at as a big reason for global warming. To reduce CO2 emissions, governments worldwide have begun to enforce bans on selling traditional ICE vehicles. This effort encourages people to switch to EVs or HEVs [2-3]. Major car companies like Hyundai, Volvo, Volkswagen, and Tesla have introduced various models of EVs and are making more of them [4]. Nevertheless, numerous challenges demand attention, including concerns regarding the range capabilities of electric vehicles on a single charge, the durability of batteries, their environmental impact, insufficient charging infrastructure, and the logistical hurdles associated with recharging or swapping batteries at electric vehicle stations [5].

Solar powered electric vehicles, also known as solar cars, have become potential solutions to address the issues faced with regular electric vehicles. These vehicles have solar panels placed on their outside, such as on the roof or built into the exterior materials. With this setup, solar-powered electric vehicles can charge themselves using solar energy while they're on the move or parked. This makes them sustainable because they lower CO2 emissions, require charging less often than regular electric vehicles, and cut down on fuel costs [6]. Several brands have released commercially available models of solar-powered electric vehicles, like the Solar Prius by Toyota, Sonata by Hyundai, Vision EQXX by Mercedes-Benz, and more [7]. It's predicted that the global market for these vehicles will surpass $4.5 billion annually by 2030 [8]. However, it's important to deal with challenges such as the lower efficiency of solar cells, limited space on vehicles for installing solar panels, and changes in power output [9]. Many

[1] * Ph.D Scholar, GITAM School of Technology, GITAM Deemed to be University, Hyderabad, Telangana & Assistant Professor/ EEE, CVR College of Engineering, Hyderabad, Telangana

[2] Assistant Professor /EEE, GITAM School of Technology, GITAM Deemed to be University, Hyderabad, Telangana

researchers are focusing on developing technologies to make solar-powered electric vehicles more commercially feasible and practical.

In [10] researchers conducted assessments on the impact of high-efficiency solar cell advancements in extending the drivable range. They also outlined potential benefits such as reduced carbon dioxide emissions, lower EV charging expenses, and decreased reliance on battery capacity with the adoption of PV-powered EVs. Japanese researchers are trying to make better and cheaper solar cells and panels for solar-powered electric vehicles. Researchers are exploring various types of solar cells to assess potential cost savings and their impact on different aspects. Moreover, extensive research has been conducted to evaluate the feasibility, effectiveness, and viability of integrating solar-powered charging stations for electric vehicles, considering both technical feasibility and financial implications.

Numerous investigations have delved into optimizing parking facilities for photovoltaic (PV)-powered electric vehicles (EVs). Researchers have projected the charging potential during parking intervals and proposed optimal parking locations through geospatial analyses, considering solar irradiation and shadow patterns at specific sites [13]. A novel approach has been developed to identify shaded areas throughout the day using a shading matrix, which illustrates the extent of shading in various areas each hour, such as roads or parking spots [14]. Additionally, researchers have assessed the accuracy of two methods: one involving modelling and another based on real-life measurements [15]. Moreover, numerous studies have explored optimal routes for solar-powered electric vehicles [16].

In a recent investigation, researchers conducted calculations to estimate the solar energy generation potential of a vehicle equipped with solar panels on its roof while traveling along a 120 km stretch of highway. Their analysis encompassed variations in sunlight intensity, shaded regions influenced by time and geographic location, as well as segments of the road passing through tunnels. In [18], scientists developed a predictive model to assess the power output of a solar bus equipped with a rooftop solar attachment. Additionally, they conducted an experimental validation to compare the model's predictions with real-world outcomes. Similarly, in [19], it was proposed to install solar panels on the roof of a train. A specialized computer program was devised to predict the generation capacity of the panels, considering fluctuations in sunlight and shadows at different times and locations during the train's operation.

However, these studies exhibit certain limitations as they primarily focus on assessing the solar power generation potential of the panels installed solely on the roof of the vehicle. Additionally, none of these studies have investigated the power generation capacity considering all four sides of the vehicle. Historically, solar-powered electric vehicles typically featured only one solar panel on the roof. However, future iterations are anticipated to incorporate solar cells on multiple parts of the vehicle, including the bonnet, rear window, left door, and right door, in addition to the roof. These cells may be designed to be see-through on glass surfaces and lighter in weight on the hood, roof, and side panels, employing a specialized configuration known as Vehicle-Integrated Photovoltaics (VIPV). Consequently, it is imperative to consider various vehicle surfaces to maximize the power generated by future photovoltaic (PV)-powered electric vehicles (EVs) [20].

This research endeavors to assess the energy generation potential of a photovoltaic (PV)-powered electric vehicle and analyze how this generation may be influenced by atmospheric conditions. Specifically, the study aims to investigate the fluctuations in (1) solar irradiation, (2) vehicle speed, and (3) load torque. Objectives of the paper are

The objectives for the provided work are as follows:

1. Introduce an electric vehicle (EV) configuration incorporating advanced MPC based on ANN technology for precise vector control of induction motors.

2. Investigate the integration of a photovoltaic (PV) array to complement the fuel cell system, utilizing excess power for electrolysis during idle periods of the vehicle.

3. Explore the application of a QBBC to manage voltage output, ensuring compatibility with various energy sources.

4. Evaluate the performance and efficiency of the proposed EV setup under diverse irradiance and speed conditions through comprehensive simulation studies.

5. Enhance converter control strategies to maintain stable DC output voltage by considering both overall voltage and individual current levels.

6. Compare the efficacy of ANN-based MPC with traditional Proportional-Integral (PI) controllers in regulating motor speed.

7. Introduce an innovative approach for torque control of AC machines utilizing ANN estimators, thereby eliminating the necessity for weighting factors.

8. Validate the effectiveness of the proposed techniques and control strategies through comparative analysis with conventional methods using MATLAB/SIMULINK simulations.

II. Proposed Electric Vehicle with Solar Onboard

Figure 1 illustrates proposed HEV configuration incorporating both on-board solar panels and fuel cells.

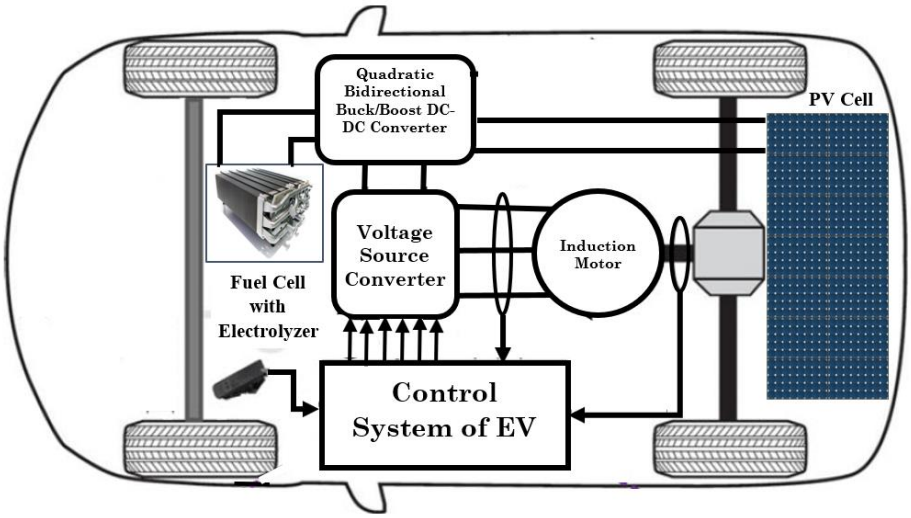

Figure 1. Proposed HEV configuration

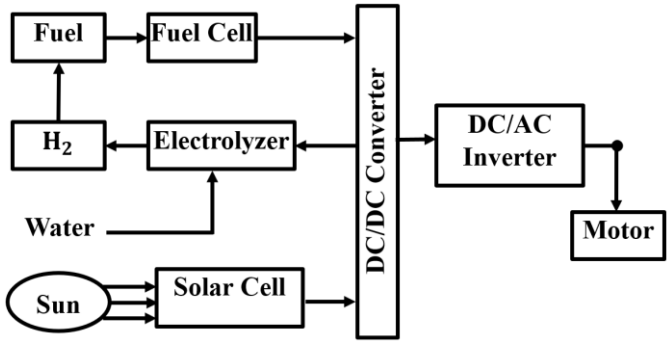

Fig 2. HEV with Solar and Fuel Cell

HEVs employ specialized converters known as DC-DC bidirectional boost-buck converters, capable of transferring power bidirectionally. Over recent years, there has been a notable surge in research concentrated on emerging high-gain boost converters, which have gained popularity in the power electronics domain due to their necessity across various applications such as fuel cells, distributed solar power generation, and backup power supplies. In these applications, achieving a relatively high gain, denoted as V_{out}/V_{in}, is crucial. However,

conventional boost converters encounter limitations hindering their ability to attain such high step-up gain. These limitations include the necessity for swift switch-off times, leading to stress on the switches due to high voltages, and inefficiency. Consequently, there is a demand for converters capable of yielding higher power gains while operating more efficiently to address these issues.

By adjusting the switch-on duration or increasing the number of coils in the connected inductor, converters can generate higher voltages. However, many of these converters exhibit drawbacks such as significant fluctuations in input current. Quadratic converters present an alternative approach to boosting the power output of conventional boost converters, garnering attention from numerous researchers in the field of power electronics.

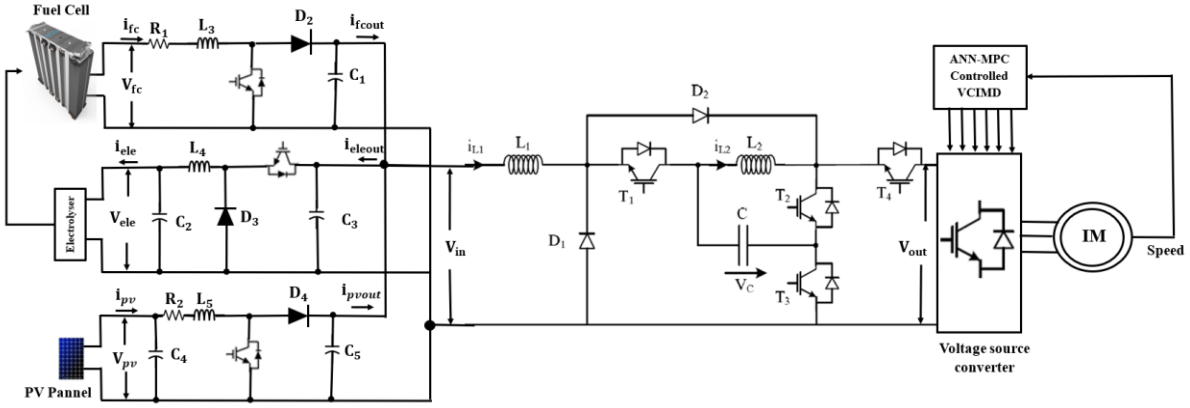

Figure 3. Schematic of proposed Electric vehicle with on board PV panels.

A. Electrolyzer

An electrolyzer is a device which utilizes electrical energy to separate water (H_2O) into its basic elements: hydrogen (H_2) and oxygen (O_2), a procedure known as electrolysis. This process involves passing an electric current through water or a salt solution, causing the water molecules to separate into hydrogen and oxygen gases. These gases can then be collected separately and used for various purposes. Hydrogen, for instance, can assist as a clean fuel for vehicles, in industrial applications, or as a source of energy in fuel cells for electricity generation. The electrolyzer operates at temperatures below 70°C to minimize material limitations, and it produces hydrogen with a purity of up to 99.9%. Hydrogen production rate of electrolysis is given as

$$X_{H_2} = \frac{5.18e^{-6} I_e mole}{s} \tag{1}$$

The flow of electricity among the electrodes is denoted by I_e, The hydrogen (H_2) is deposited in a tank. The stored hydrogen serves as a backup power source for generating electricity during periods of low sunlight availability, after which it is directed into the fuel cell (FC).

B. Fuel cell

A fuel cell is a specialized device that transforms the energy stored in a fuel, typically hydrogen, directly into electricity through a unique chemical reaction. Functioning like a battery, a fuel cell requires a constant supply of fuel and a reactant, typically oxygen from the air, to sustain the chemical reactions. In the various types of fuel cells, the proton exchange membrane fuel cell (PEMFC) is the highest prevalent. Operating at relatively low temperatures, typically between 50°C to 100°C, PEMFCs find applications in diverse areas such as automotive propulsion, stationary power generation for buildings, and portable electronic devices.

The Nernst equation relates the electrical working of the fuel cell to certain conditions under atmospheric pressure [13].

$$V_o = E_o + \frac{R.T}{2F} \ln \frac{x_{H_2} {x_{O_2}}^{0.5}}{x_{H_2O}} \tag{2}$$

A detailed discussion on the photovoltaic (PV) generation system, incorporating an incremental conductance-based maximum power point tracking (MPPT) algorithm, alongside a fuel cell integrated with a DC-DC converter is explained in [14].

C. Quadratic bidirectional boost /buck DC-DC Converter

Figure 4 depicts the topology of the QBBC. This topology eliminates the need for additional passive components like inductors and capacitors, setting it apart from the classical Boost quadratic converter [15]. The QBBC shows a static voltage gain, employing a quadratic function for both Buck and Boost operating modes. Charging or discharging of the converter is facilitated by one switch.

During the forward mode, the QBBC functions as a Boost converter, facilitating the transfer of power from the input side to the output side. Two IGBTs (T_1 and T_4) remain in the OFF state consistently, while the IGBT (T_3) remains in the ON state continuously. Pulse Width Modulation (PWM) with a switching time of T_C can be applied to T_2, utilizing output voltage control and inner current control. During Boost mode, when the IGBT T_2 is in the ON state (during the time interval of ΔT_S), the inductors L_1 and L_2will be charged with linearly rising current, transferring energy stored in the capacitor C to the inductor L_2. Conversely, when the IGBT T_2 is in the OFF state, the inductors L_1 and L_2 will be discharged with linearly decreasing current, transferring energy stored in the inductors to the capacitor and output side.

$$\Delta V_{in} + (1-\Delta)(V_{in} - V_c) = 0 \tag{3}$$

$$\Delta V_c + (1-\Delta)(V_c - V_{out}) = 0 \tag{4}$$

Then voltage gain is given as

$$G = \frac{V_{out}}{V_{in}} = \frac{1}{(1-\Delta)^2} \tag{5}$$

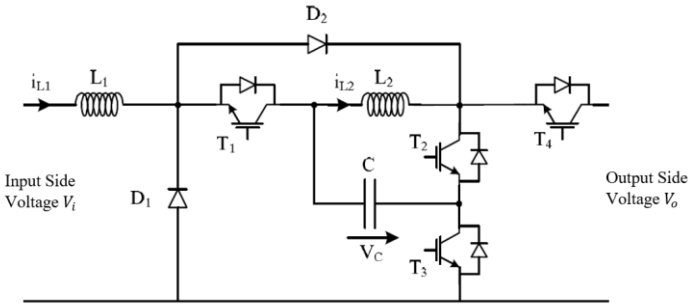

Figure 4. QBBC schematic

In reverse mode, the converter transfers energy from the output side to the input side, functioning as a Buck converter. During this mode of operation, the IGBTs T_2 and T_3 remain in the OFF state, while the IGBT T_4 remains in the ON state. PWM with a switching time of T_c can be applied to T_1 using output voltage control and inner current control. When T_1 is in the ON state (during the time interval of ΔT_S), the currents in inductors L_1 and L_2 will increase linearly as capacitor C discharges, transferring its energy to inductor L_1. When T_1 is in the OFF state (during the time interval of 1-ΔT_S), the currents in inductors L_1 and L_2 will decrease linearly, and the energy stored in the inductors will be transferred to the capacitor C and to the input side.

During Buck Mode

$$\Delta(V_c - V_{in}) - (1-\Delta)V_{in} = 0 \tag{6}$$

$$\Delta(V_c - V_{out}) + (1-\Delta)V_c = 0 \tag{7}$$

Then voltage gain is given as

$$G = \frac{V_{in}}{V_{out}} = \Delta^2 \tag{8}$$

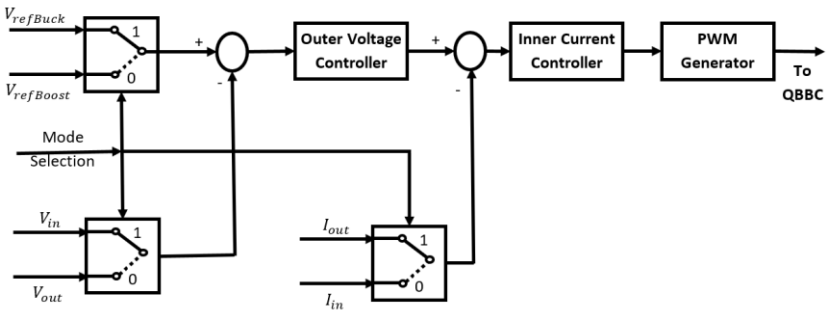

Figure 5. Controlling of QBBC

Figure 3 illustrates the control strategy of the QBBC, functioning in both boost and buck modes. The selection of mode, whether buck or boost, is dependent upon the direction of power flow or current. Control of the DC-DC converter entails the utilization of two loops: one for voltage control and another for current management. These loops incorporate Proportional-Integral (PI) controllers to ensure the stability of both voltage and current. Here are the advantages of this converter:

• Due to its minimal fluctuation in input current and reduced energy losses during electricity flow, this converter is well-suited for low to medium power requirements.

• Compared to a standard quadratic boost converter, this converter is capable of significantly higher voltage boosting.

• With the same output voltage, this converter imposes less strain on the primary device compared to a conventional converter.

III. VECTOR CONTROL OF INDUCTION MOTOR

Scalar control, although simple to implement, encounters challenges regarding the interaction between flux and torque in induction machines. This interaction can result in sluggish and occasionally unstable responses due to complex system effects. Adjusting torque by controlling slip or frequency often leads to a gradual decrease in flux. To counteract this flux reduction, a flux control loop is activated. However, this loop operates with a significant time constant, causing a momentary dip in flux and reducing torque sensitivity with slip, consequently prolonging response times. Unlike DC motor drives, where flux control is independent due to separately excited field windings, controlling induction motor drives requires adjustments of stator current, frequency, and phase angle, making it a more intricate task. Through the application of inverter control and field-oriented control techniques, AC drives can attain independent regulation of flux and torque, similar to DC drives, by controlling the phase, frequency, and magnitude of currents in field coordinates. This strategy, referred to as vector control, facilitates precise control of flux phasors and enhances the overall performance of AC motor drives.

A. Principle of Vector Control

Vector control involves determining the position of the rotor flux linkage phasor λ_r. The phasor diagram is illustrated in Figure 6.

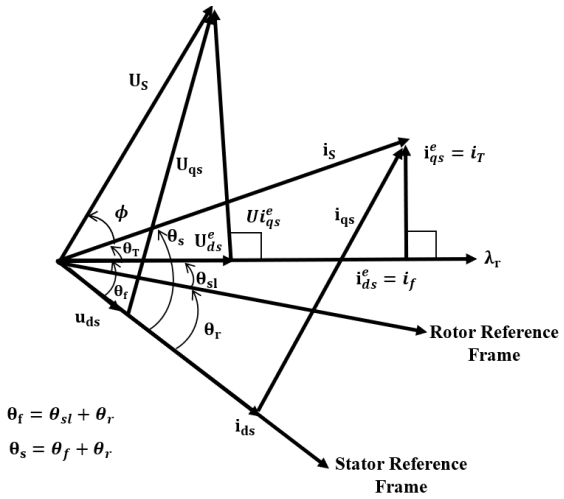

Figure 6. phasor diagram

Here, λ_r is positioned at an angle θ_f from the stationary reference, known as the flux angle. The stator currents can be changed into q and d axis using

$$\begin{bmatrix} i_{qs} \\ i_{ds} \end{bmatrix} = \frac{2}{3}\begin{bmatrix} cos\theta_f & cos\left(\theta_f - \frac{2\pi}{3}\right) & cos\left(\theta_f + \frac{2\pi}{3}\right) \\ sin\theta_f & sin\left(\theta_f - \frac{2\pi}{3}\right) & sin\left(\theta_f + \frac{2\pi}{3}\right) \end{bmatrix}\begin{bmatrix} i_{as} \\ i_{bs} \\ i_{cs} \end{bmatrix} \tag{9}$$

from which the stator current phasor i_s derived as

$$|i_s| = \sqrt{(i_{ds})^2 + (i_{qs})^2} \tag{10}$$

and the stator phase angle is

$$\theta_s = tan^{-1}\left(\frac{i_{qs}}{i_{ds}}\right) \tag{11}$$

where i_{qs} and i_{ds} are the 'q' and 'd' axes currents. The magnitude of the current phasor remains constant whatever the reference frame selected.

The stator current generates the rotor flux i_s and the torque λ_r.The component of current generating the rotor flux is in phase with λ_r. Hence, dividing the stator current phasor along i_f discloses that this component is the flux producing component and the perpendicular component is thus the torque-producing component i_T .

$$\lambda_r \propto i_f \tag{12}$$

$$T_e \propto \lambda_r i_T \propto i_f i_T \tag{13}$$

The i_f and i_T are DC components,

Flux angle can be expressed as:

$$\theta_f = \theta_{sl} + \theta_r \tag{14}$$

In this equation, θ_r is the rotor position, and θ_{sl} is the slip angle. In terms of speeds and time, the flux angle is

$$\theta_f = \int(\omega_{sl} + \omega_r)dt = \int(\omega_s)dt \tag{15}$$

Vector control methods depends on accuracy in determining the position of the rotor's magnetic field at any given moment and are classified into direct and indirect approaches. In direct vector control, the field angle is determined using stator voltages and currents, or specialized windings designed to detect the magnetic field.

B. Indirect Vector Control for Induction Motor

The dynamic equations of the induction motor in the synchronous reference frame, considering the rotor flux as the state variable, are given as follows:

$$r_r\, i_{qr} + p\lambda_{qr} + \omega_{sl}\lambda_{dr} = 0 \tag{16}$$

$$r_r\, i_{dr} + p\lambda_{dr} + \omega_{sl}\lambda_{qr} = 0 \tag{17}$$

Where

$$\omega_{sl} = \omega_s - \omega_r \tag{18}$$

$$\lambda_{qr} = L_r\, i_{qr} + L_m\, i_{qs} \tag{19}$$

$$\lambda_{dr} = L_r\, i_{qr} + L_m\, i_{ds} \tag{20}$$

The resultant rotor flux linkage λ_r, is supposed to be aligned with the direct axis to accomplish field orientation. This orientation reduces the number of variables to be dealt with.

The position of the d-axis with rotor flux phasor yields

$$\lambda_r = \lambda_{dr} \tag{21}$$

$$\lambda_{qr} = 0 \tag{22}$$

$$p\lambda_{qr} = 0 \tag{23}$$

Substituting Equations 19 to 20 into Equations 22 and 23 yields the new rotor equations as follows:

$$r_r\, i_{qr} + \omega_{sl}\lambda_r = 0 \tag{24}$$

$$r_r\, i_{dr} + p\lambda_{dr} = 0 \tag{25}$$

Thus, from Equations 24 and 25, the rotor currents are derived as follows:

$$i_{qr} = \frac{-L_m}{L_r}\, i_{qs} \tag{26}$$

$$i_{dr} = \frac{\lambda_r - L_m\, i_{ds}}{L_r} \tag{27}$$

Substituting the expressions for the *d* and *q* axis rotor currents

$$i_f = \frac{1}{L_r}[1 + pT_r]\lambda_r \tag{28}$$

$$\omega_{sl} = -\frac{r_r\, i_{qr}}{\lambda_r} = \frac{L_m}{T_r}\frac{i_T}{\lambda_r} \tag{29}$$

Where

$$i_T = i_{qs} \tag{30}$$

$$i_F = i_{ds} \tag{31}$$

$$T_r = \frac{L_r}{r_r} \tag{32}$$

$$K_{it} = \frac{4}{3p} \tag{33}$$

By substituting the rotor currents, the torque expression can be obtained as:

$$T_e = \frac{3P}{4}\frac{L_m}{L_r}\left(\lambda_{dr}\, i_{qs} - \lambda_{qr}\, i_{ds}\right) = \frac{3P}{4}\frac{L_m}{L_r}\left(\lambda_{dr}\, i_{qs}\right) = K_{te}\left(\lambda_r\, i_{qs}\right) \tag{34}$$

The stator current phasor is the sum of the 'd' and the 'q' axes stator currents in any reference frame, given as:

$$i_s = \sqrt{(i_{ds})^2 + \left(i_{qs}\right)^2} \tag{35}$$

C. Indirect Vector Control

Figure 7 shows the indirect vector control with ANN speed estimation and MPC controller.

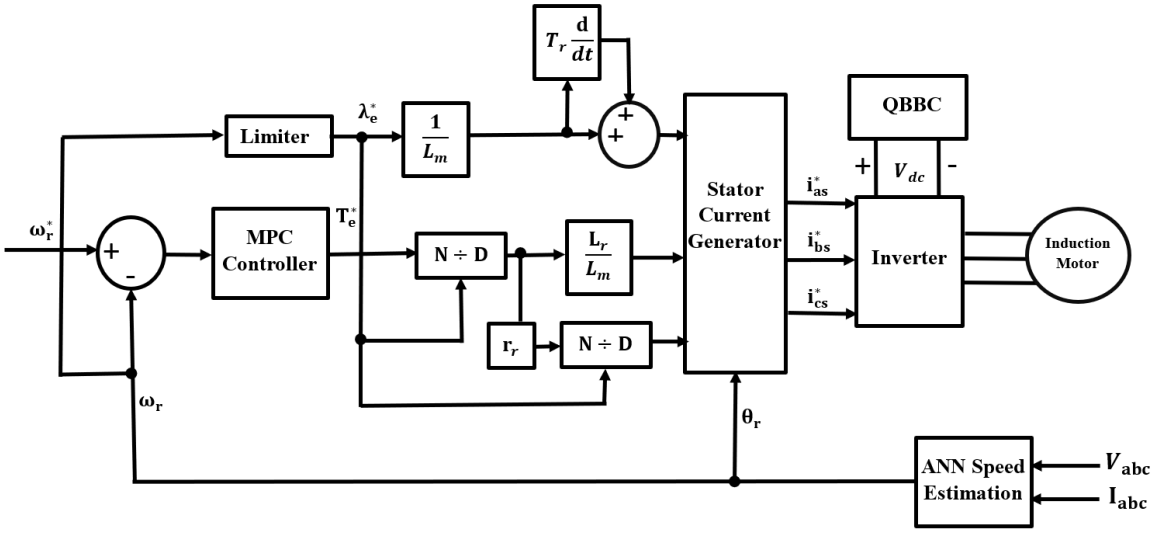

Figure 7. Implementation of the indirect vector control

In a simple drive strategy, the flux command is typically set as a function of speed.

$$\lambda_r{}^* = \lambda_b \quad 0 \le |\omega_r| \le \omega_{rated} \tag{36}$$

$$= \frac{\omega_b}{|\omega_r|}\lambda_b \quad \omega_b \le |\omega_r| \le \omega_{r(max)} \tag{37}$$

Here, λ_b and ω_r represent base rotor flux and rotor speed, separately. The flux is kept at the rated value until the rated speed is reached; beyond that, the flux is lowered to keep the power output constant. Following the control scheme depicted in Figure 7, the commands for the three-phase stator currents are generated. Three phase stator source currents are assessed with actual stator currents to make the pulses by using hysteresis pulse width modulation.

IV. MPC

A. Inverter Model

This study employs the two-level voltage source inverter (2L-VSI), as the desired inverter topology. Despite its tendency to generate significant harmonic content, the 2L-VSI is favoured for its simplicity and versatile power conversion capabilities. Each output leg of the 2L-VSI comprises only two power switches that operate

complementarily. Among these vectors, v_0 and v_7 represent null voltage vectors, where ($v_\alpha = 0$; $v_\beta = 0$). Given the emphasis of this work on control strategy, the decision to utilize this straightforward inverter is preferred.

The equations presiding the operation of the 2L-VSI are as follows:

$$v_a = S_a \frac{V_{dc}}{2} \tag{38}$$

$$v_b = S_b \frac{V_{dc}}{2} \tag{39}$$

$$v_c = S_c \frac{V_{dc}}{2} \tag{40}$$

The voltage in $\alpha - \beta$ frame can be as

$$\begin{bmatrix} v_\alpha \\ v_\beta \end{bmatrix} = \frac{2}{3} V_{dc} \begin{bmatrix} 1 & -0.5 & -0.5 \\ 0 & \sqrt{3}/2 & -\sqrt{3}/2 \end{bmatrix} \begin{bmatrix} S_a \\ S_b \\ S_c \end{bmatrix} \tag{41}$$

B. Motor Model

In the mathematical model of the induction motor (IM), the state variables include the stator flux (Ψs) and stator current (i_s). When represented in a stationary frame, the dynamic equations of the IM can be expressed as follows:

$$v_s = r_s i_s + \frac{d\lambda_s}{dt} \tag{42}$$

$$0 = r_s i_r + \frac{d\lambda_r}{dt} - j\frac{\omega_r}{p}\lambda_r \tag{43}$$

$$\lambda_s = L_s i_s + L_m i_r \tag{44}$$

$$\lambda_r = L_m i_s + L_r i_r \tag{45}$$

$$T = \frac{3}{2} p |\lambda_s \otimes i_s| \tag{46}$$

$$J\frac{d\omega_r}{dt} = T_e - T_L \tag{47}$$

To predict the torque and flux accurately, it's essential to estimate the stator flux $\lambda_s$and the rotor flux $\lambda_r$at the current sampling time (k). The rotor flux can be determined using the pertinent equation of the rotor dynamics of an induction motor (IM) in a rotating reference frame aligned with the rotor winding, expressed as:

$$\psi_r + \tau_r \frac{d\psi_r}{dt} = L_m i_s \tag{48}$$

The rotor time constant $\tau_r = L_r/R_r$is critical. Employing backward-Euler discretization with the sampling time T_s,the discrete-time equation for estimating the rotor flux is represented as:

$$\lambda_r^k = L_m \frac{T_s}{T_r} i_s^{k-1} + \left(1 - \frac{T_s}{T_r}\right)\lambda_r^{k-1} \tag{49}$$

The stator flux can be valued by

$$\lambda_s^k = \frac{L_m}{L_r}\lambda_r^k + \left(1 - \frac{L_m^2}{L_s L_r}\right) i_s^k \tag{50}$$

$$\lambda_s^k = \frac{L_m}{L_r}\lambda_r^k + \left(1 - \frac{L_m^2}{L_s L_r}\right) i_s^k \tag{51}$$

Now, the stator flux using the forward-Euler discretization:

$$\lambda_s^{k+1} = \lambda_s^k + T_s v_s^k - T_s R_s i_s^k \tag{52}$$

the stator current using the forward-Euler discretization:

$$i_s^{k+1} = C_1 i_s^k + C_2 \lambda_s^k + \frac{T_s}{L_\sigma} v_s^k \tag{53}$$

where $R_\sigma = (R_s + (L_m/L_r)^2 R_r)$ relates to the equivalent resistance, $C_1 = (1 - (R_\sigma T_s/L_\sigma))$, $L_\sigma = \sigma L_s$ is the leakage inductance of the system and

$$C_2 = \frac{(L_m/L_r)T_s}{L_\sigma\left((1/\tau_r) - j\omega^k\right)} \tag{54}$$

Finally, the torque prediction depends on the forecasted values of the stator flux and stator current, given by the following equations.

$$T^{k+1} = \frac{3}{2} p|\lambda_s^{k+1} \otimes i_s^{k+1}| \tag{55}$$

C. Online ANN Speed Estimator

From the mathematical modelling of the induction motor, we derive the equations governing its behaviour and performance.

$$\begin{bmatrix} v_{ds} \\ v_{qs} \\ 0 \\ 0 \end{bmatrix} = \begin{bmatrix} r_s + L_s\frac{d}{dt} & 0 & L_m\frac{d}{dt} & 0 \\ 0 & r_s + L_s\frac{d}{dt} & 0 & L_m\frac{d}{dt} \\ L_s\frac{d}{dt} & \omega_r L_m & r_r + L_r\frac{d}{dt} & \omega_r L_r \\ -\omega_r L_m & L_m\frac{d}{dt} & -\omega_r L_r & r_r + L_r\frac{d}{dt} \end{bmatrix} \begin{bmatrix} i_{ds} \\ i_{qs} \\ i_{dr} \\ i_{qr} \end{bmatrix} \tag{56}$$

Stator current can be estimated as

$$\frac{d}{dt}\begin{bmatrix} \hat{\imath}_{ds} \\ \hat{\imath}_{qs} \end{bmatrix} = \begin{bmatrix} -\frac{r_s^*}{L_\sigma} & -\omega_r & \frac{r_r}{L_\sigma L_r} & \frac{\omega_r}{L_\sigma} \\ \omega & -\frac{r_s^*}{L_\sigma} & \frac{\omega_r}{L_\sigma} & \frac{r_r}{L_\sigma L_r} \end{bmatrix} \begin{bmatrix} \hat{\imath}_{ds} \\ \hat{\imath}_{qs} \\ \hat{\lambda}_{ds} \\ \hat{\lambda}_{qs} \end{bmatrix} + \frac{1}{L_\sigma}\begin{bmatrix} v_{ds} \\ v_{qs} \end{bmatrix} \tag{57}$$

By employing the forward rectangular rule and reorganizing the resultant equation into a format suitable for implementation in an ANN, we express the discrete-time estimation of the stator current as follows:

$$\begin{bmatrix} \hat{\imath}_{sd}^k \\ \hat{\imath}_{sq}^k \end{bmatrix} = \left(1 - \frac{T_s r_s^*}{L_\sigma}\right)\begin{bmatrix} \hat{\imath}_{sd}^{k-1} \\ \hat{\imath}_{sd}^{k-1} \end{bmatrix} + \frac{T_s \omega_r}{L_\sigma}\begin{bmatrix} \hat{x}_{sd}^{k-1} \\ \hat{x}_{sq}^{k-1} \end{bmatrix} + \frac{T_s r_r}{L_\sigma L_r}\begin{bmatrix} \hat{\lambda}_{sd}^{k-1} \\ \hat{\lambda}_{sq}^{k-1} \end{bmatrix} + \frac{T_s}{L_\sigma}\begin{bmatrix} v_{ds}^{k-1} \\ v_{qs}^{k-1} \end{bmatrix} \tag{58}$$

This equation can be simplified as:

$$\vec{\imath}_s^k = w_1\vec{x}_1 + w_2\vec{x}_2 + w_3\vec{x}_3 + w_4\vec{x}_4 \tag{59}$$

Where $w_1 = \left(1 - \frac{T_s r_s^*}{L_\sigma}\right)$, $\vec{x}_1 = \begin{bmatrix} i_{sd}^{k-1} \\ i_{sd}^{k-1} \end{bmatrix}$, $w_2 = \frac{T_s \omega_r}{L_\sigma}$, $\vec{x}_2 = \begin{bmatrix} \hat{x}_{sd}^{k-1} \\ \hat{x}_{sq}^{k-1} \end{bmatrix}$, $w_3 = \frac{T_s r_r}{L_\sigma L_r}$, $\vec{x}_3 = \begin{bmatrix} \hat{\lambda}_{sd}^{k-1} \\ \hat{\lambda}_{sq}^{k-1} \end{bmatrix}$, $w_4 = \frac{T_s}{L_\sigma}$ and $\vec{x}_4 = \begin{bmatrix} v_{ds}^{k-1} \\ v_{qs}^{k-1} \end{bmatrix}$ (60)

Equation (60) sets up the structure of the ANN with two layers: the input layer and the output layer. Therefore, the Widrow-Hoff learning rule by this ANN setup. This learning technique offers a straightforward weight update equation, enhancing its suitability for online speed estimation in comparison to other learning methods. Therefore, the weight w_2 in Equation (60), which encapsulates the speed, will be continuously altered online using the Windrow–Hoff learning rule. This adjustment is done to reduce the total amount of error by the measured stator current and the predicted stator current. The error at each sampling time, *k*, is calculated using the energy function, which adds up the squared differences between the measured and predicted stator currents.

$$E = \frac{1}{2}\left(\left(i_{sd}^k - \hat{\imath}_{sd}^k\right)^2 + \left(i_{sq}^k - \hat{\imath}_{sq}^k\right)^2\right) \quad (61)$$

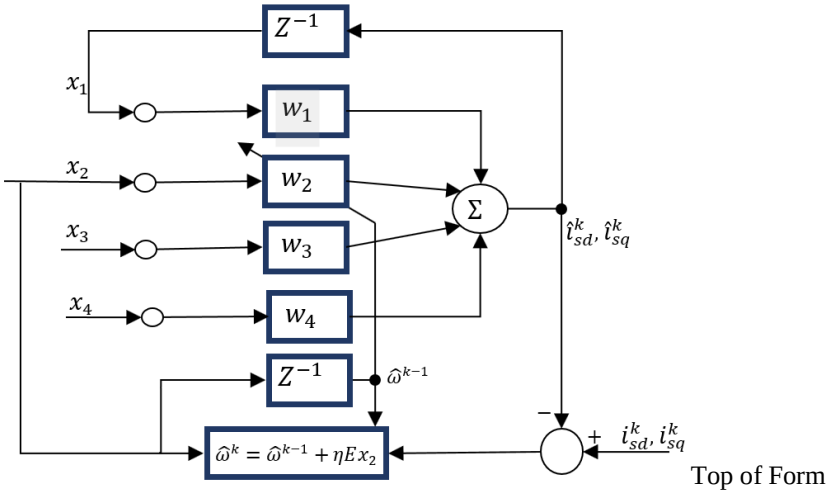

Top of Form

Figure 8. The block diagram of the proposed online ANN speed estimator

In Equation (59), only the weight w_2 is changed as the process goes on. So, how accurate the estimated stator current is largely depending on how well the assessed speed converges. The speed estimate in Equation (59) works like a low-pass filter, with a time constant that is in reverse to the learning rate. To ensure stability, a positive learning rate is employed. A smaller learning rate results in gradual conjunction, while a larger learning rate speeds up convergence but might introduce fluctuations in the estimated speed. Therefore, careful selection of the learning rate is crucial to maintain stability in the estimation system.

V. SIMULINK MODEL OF PROPOSED SYSTEM

The envisioned system of a HEV equipped with an onboard Photovoltaic (PV) array, regulated by an ANN-based MPC system, is simulated using MATLAB/SIMULINK. In this proposed HEV configuration, the fuel cell functions as the primary power source for the electric vehicle, supplemented by the onboard solar cells as a secondary source. During braking or deceleration of the induction machine, the generated energy is captured and collected in a hydrogen tank, transforming electrical energy into chemical energy through an electrolyzer. For motor speed regulation, a sensor less indirect vector control technique is employed, utilizing MPC for speed control. The MPC algorithm is tailored specifically for motor speed control, with an ANN incorporated to estimate the speed of the induction motor. To assess the effectiveness of this proposed structure, the simulation considers variations in irradiation, velocity, and force.

A. CASE 1:

In this scenario, the PV arrays are maintained at a consistent level of sunlight, while different speeds are tested to assess the working of the proposed HEV. An irradiance level of 1000 W/m^2 is sustained from 0 to 20 seconds during simulation. Concurrently, the vehicle's reference speed experiences fluctuations: 100 rad/s from 0 to 5 seconds, 120 rad/s from 5 to 10 seconds, 90 rad/s from 10 to 15 seconds, and 70 rad/s from 15 to 20 seconds. Figure 9 illustrates the intensity data, while Figure 10a depicts the voltage, current, and power generated by the solar panels during the constant irradiance period.

To enhance adaptability to changing environmental conditions, the Incremental Conductance algorithm is employed for Maximum Power Point Tracking (MPPT). When the irradiation reaches 1000 W/m^2, the solar panels generate a power output of 2.01 kilowatts. Figure 10b displays the power, voltage and current produced by the PV converter. Figure 11a depicts the power, voltage and current generated by the fuel cell, while Figure 11b illustrates the power, voltage and current of the fuel cell converter. Figure 12 presents the power, voltage and current of the electrolyzer. In Figure 13(a), the input and output voltages of the QBBC converter are shown. The QBBC converter plays a critical role in increasing the input voltage from 400V to 780V, which is necessary for powering the vehicle. The Total Harmonic Distortion (THD) in the stator current decreases from 5.3% under PI control to 2.8% with the adoption of ANN MPC control. Figure 14 demonstrates the speed and torque of the vehicle drive under both PI control and ANN MPC control, indicating that with ANN MPC control, peak overshot, rise time, and stability time are reduced compared to PI control.

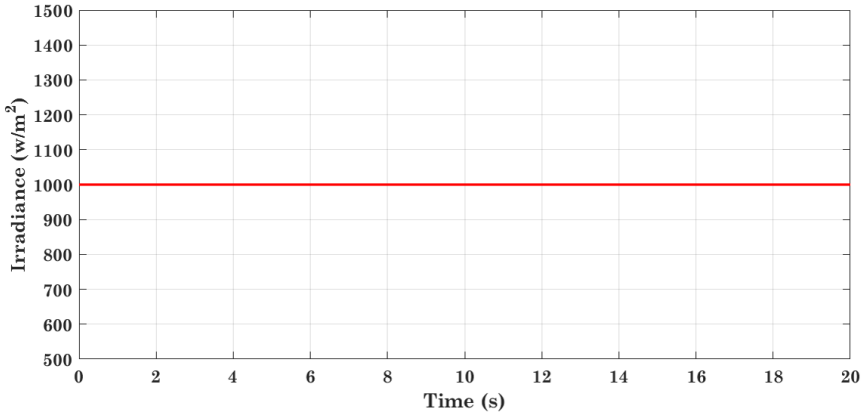

Figure 9. Irradiance of PV cells

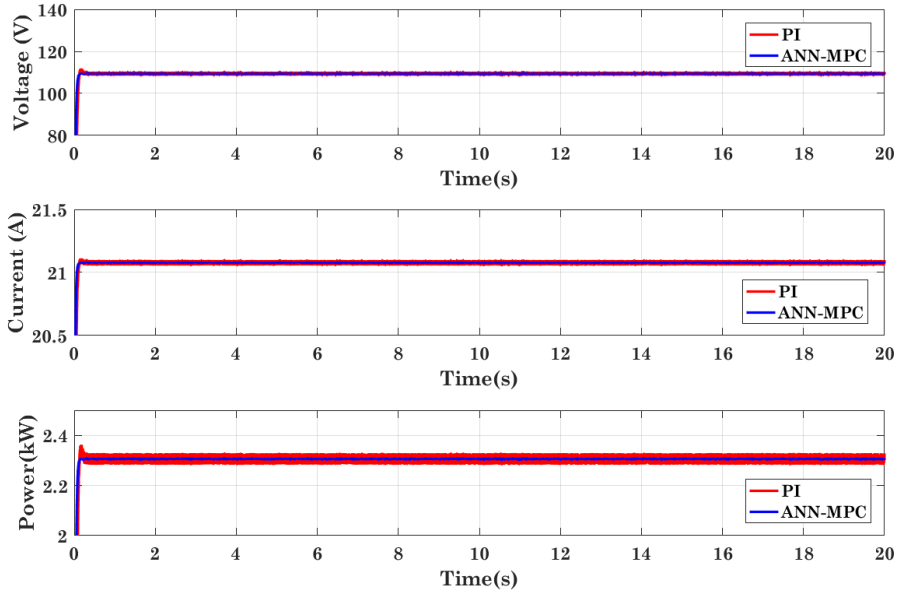

(a)

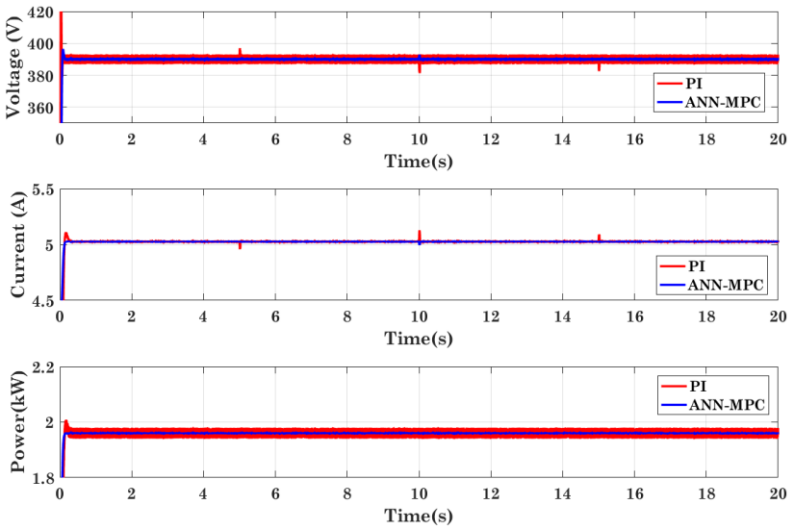

(b)

Figure 10. PV Cells Voltage and current (a) PV output voltage, current and power (b) PV converter output voltage, current and power

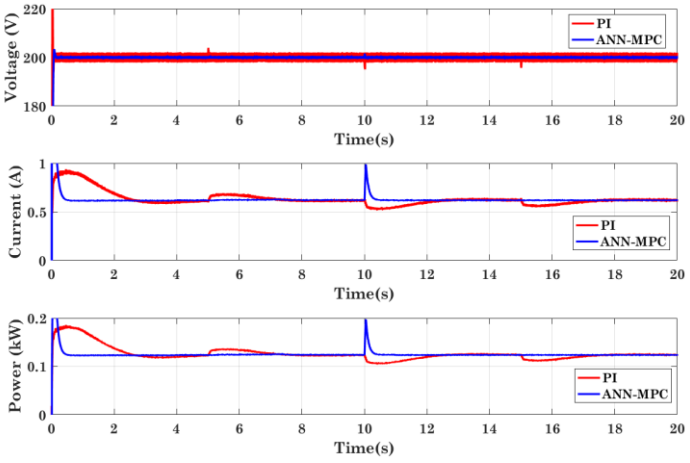

(a)

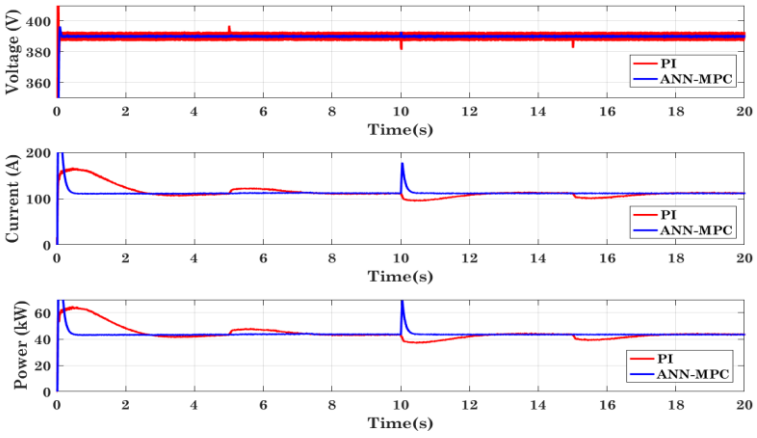

(b)

Figure 11. Fuel Cell Voltage and current (a) FC output voltage and power (b) FC converter output voltage, current and power.

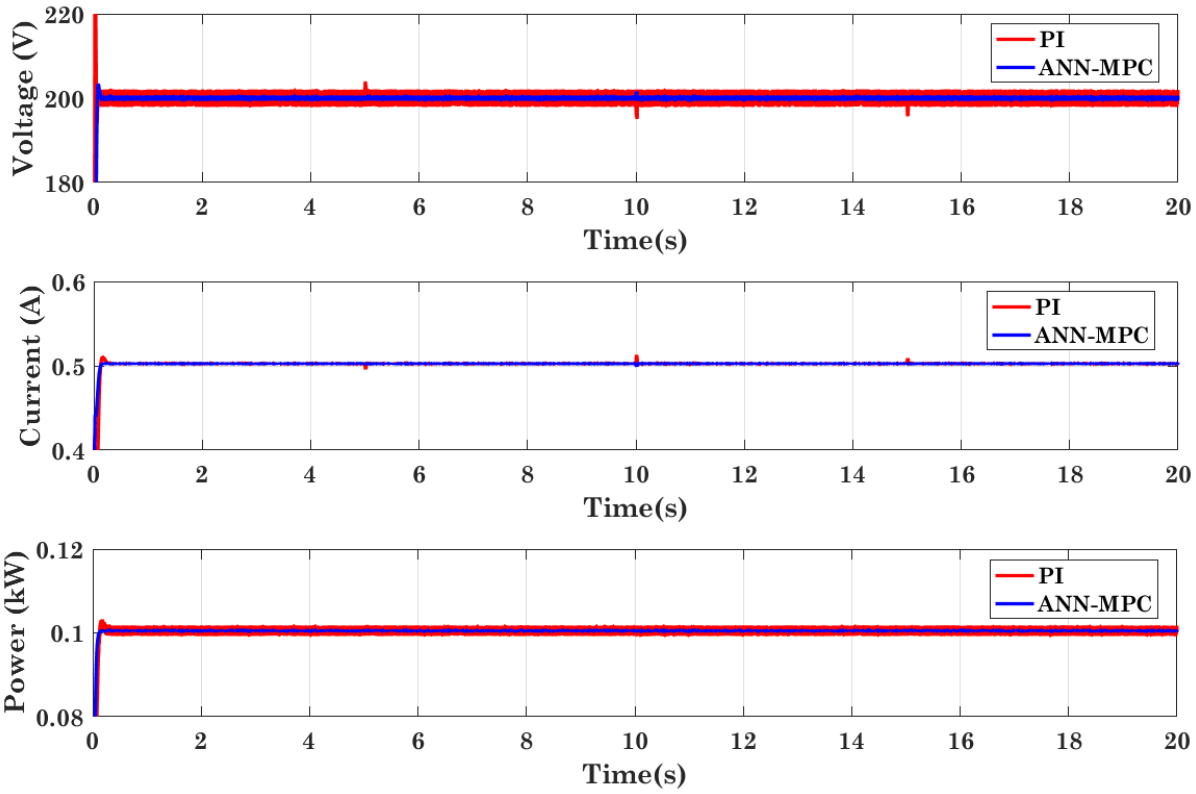

(a)

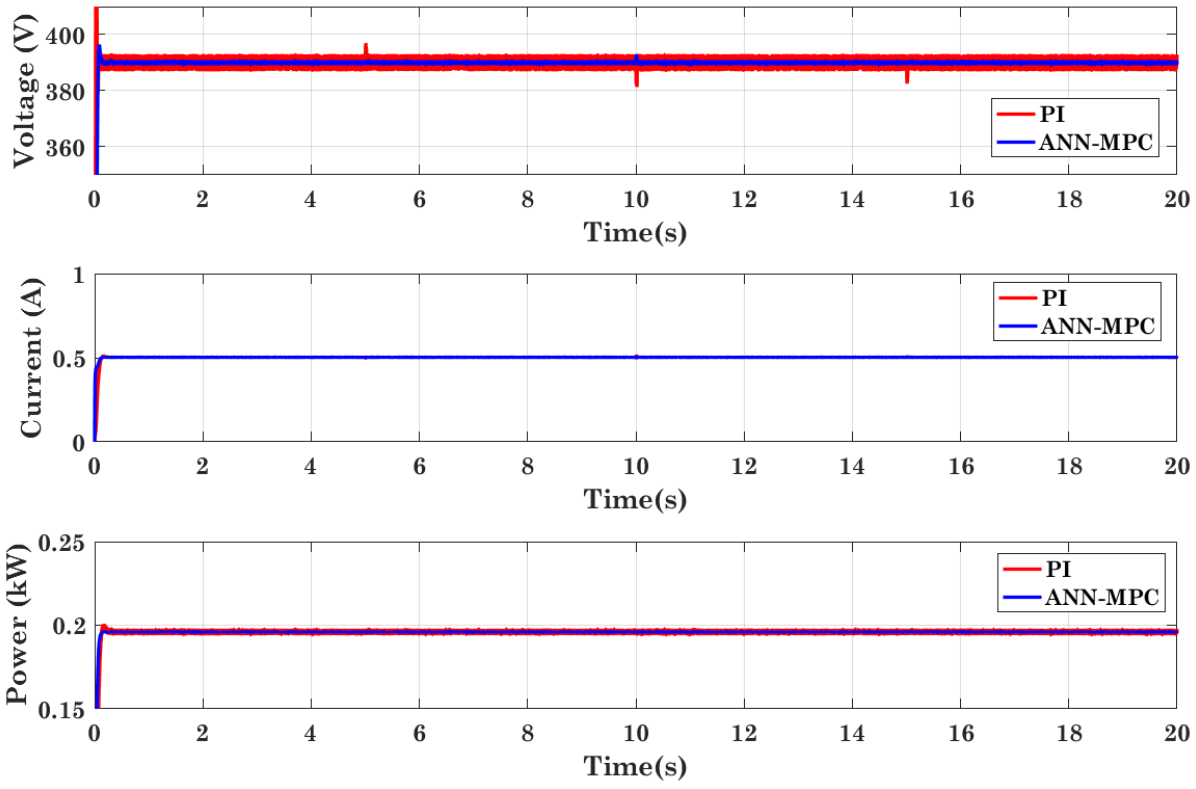

(b)

Figure 12. Electrolyzer Voltage and current (a) Electrolyzer voltage, current and power (b) Electrolyzer converter input voltage, current and power

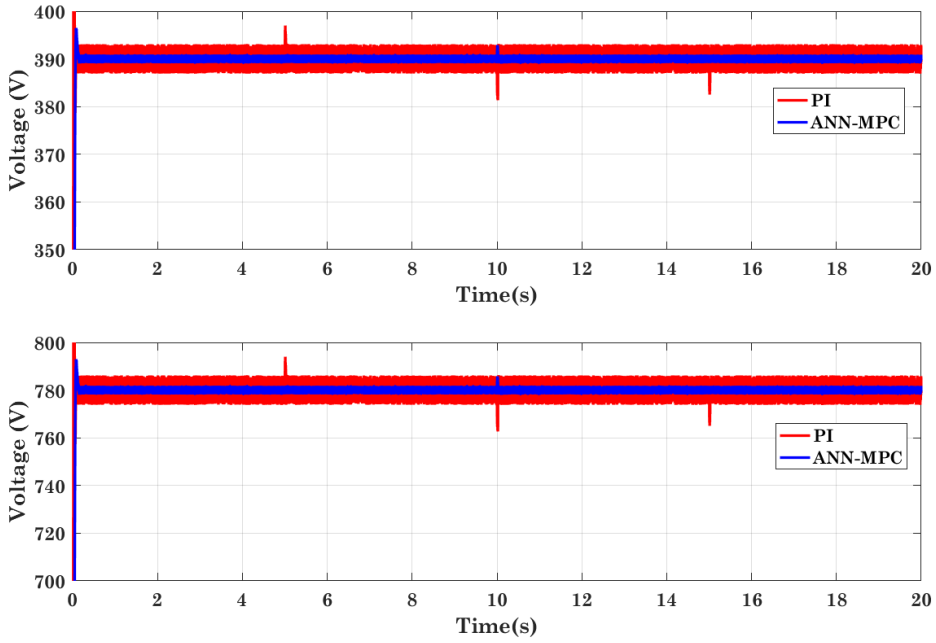

Figure 13. QBBC input voltage and output voltage

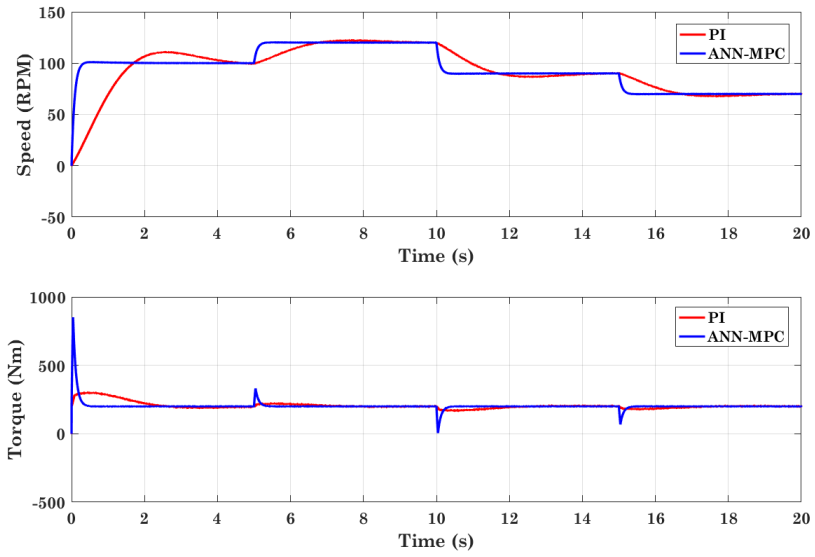

Figure 14. Motor Speed and Torque with PI Control and with Proposed ANN-MPC Control

CASE2: In the evaluation of the proposed electric vehicle (EV) configuration, the assessment considers varying irradiation conditions and changing speeds. Throughout the simulation, the reference speed in the vector control undergoes a sequence of variations: 50 rad/s, 80 rad/s, 100 rad/s, 110 rad/s, 120 rad/s, 90 rad/s, and 70 rad/s at the time instances of 0, 1, 4, 7, 10, 13, and 16 seconds, respectively. Simultaneously, the irradiance experiences the following fluctuations: $300\ W/m^2, 500\ W/m^2, 700\ W/m^2, 900\ W/m^2, 1100\ W/m^2, 1000\ W/m^2, 800\ W/m^2, 600\ W/m^2, 400\ W/m^2$, and finally $200\ W/m^2$ during the timing instants of 0, 2, 4, 6, 8, 10, 12, 14, 16, and 18 seconds, respectively. Figure 15 displays the variations in irradiation. Figure 16(a) presents the output power, voltage and current from the solar panel, while Figure 16(b) illustrates the output voltage, current, and power of the solar power system converter. In Figure 17(a), the output voltage, current, and power from the fuel cell are depicted, while Figure 17(b) showcases the output voltage, current, and power of the fuel cell converter. Figure 18(a) exhibits the output power, voltage and current at the electrolyzer, whereas Figure 18(b) portrays the output power, voltage and current of the electrolyzer converter. In Figure 19(a), both the input voltage and the boosted output voltage of the QBBC converter are presented. The QBBC converter plays a crucial role in regulating and

increasing the output voltage, ensuring that changes in irradiation on the PV cell do not impact the output voltage sent to the vehicle drive inverter. Figure 20 illustrates the motor speed and torque under both PI control and the proposed control scheme. This comprehensive set of figures provides detailed insights into the performance and behaviour of the EV system under varying irradiance conditions and changing speeds, highlighting the effectiveness of the control strategies implemented.

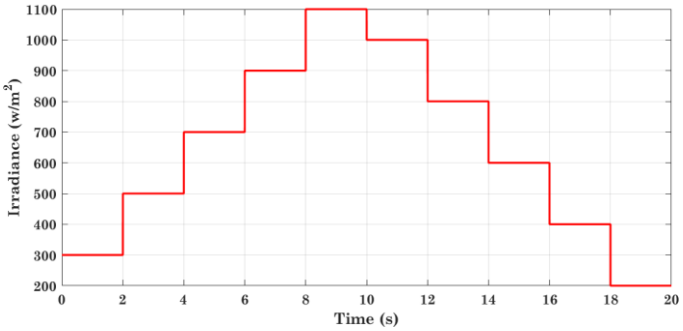

Figure 15. Irradiance of PV cells

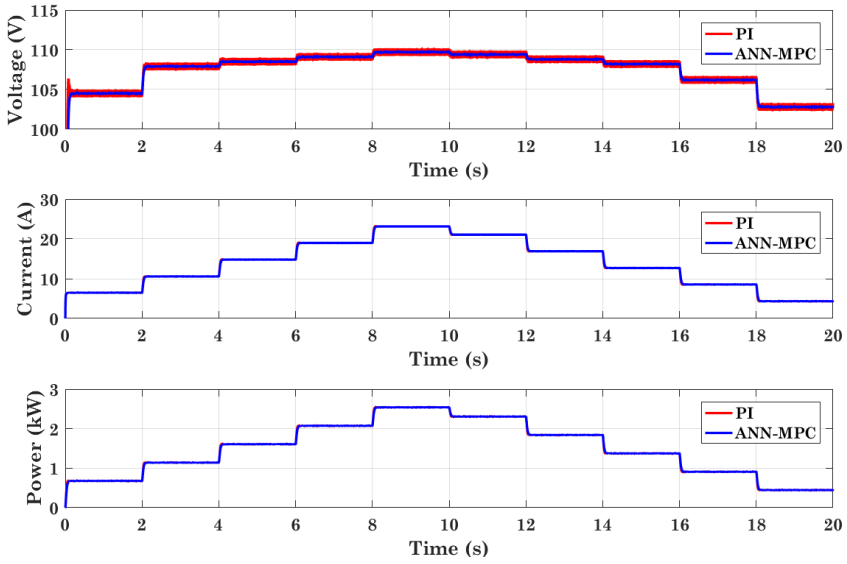

(a)

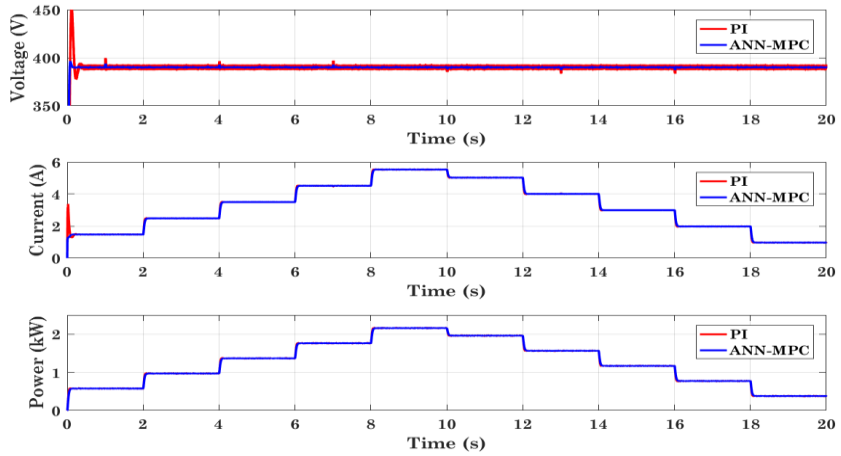

(b)

Figure 16. PV Cells Voltage and current (a) PV output voltage and power (b) PV converter output voltage, current and power

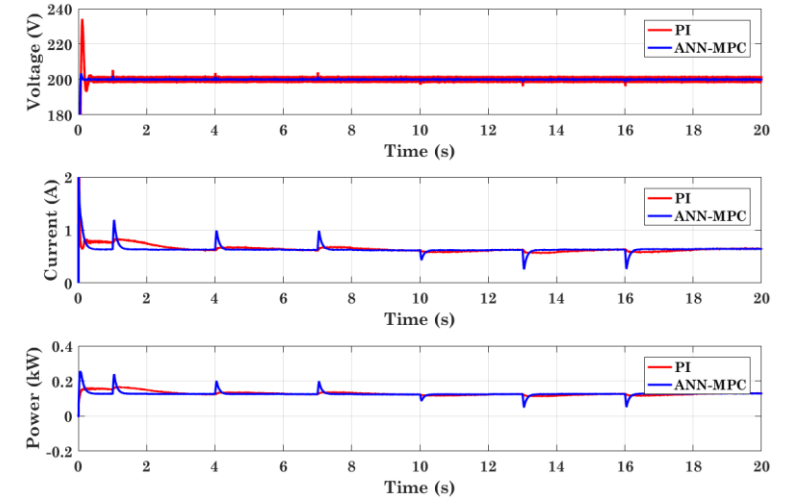

(a)

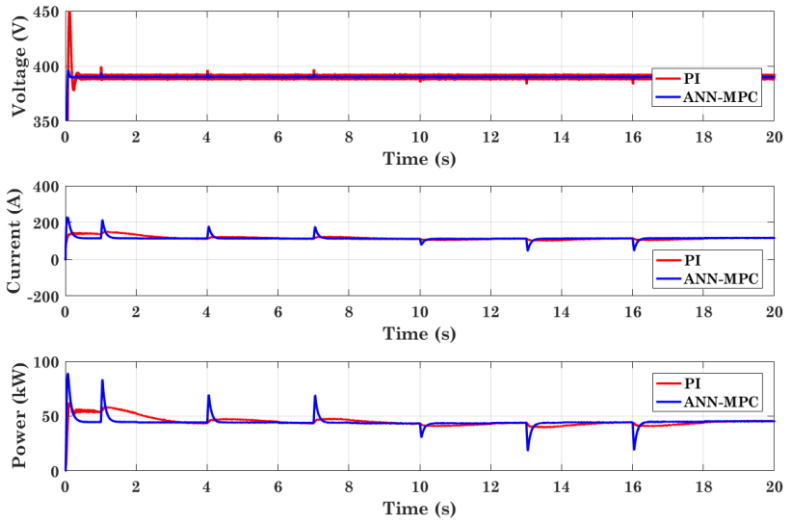

(b)

Figure 17. Fuel Cell Voltage and current (a) FC output voltage and power (b) FC converter output voltage, current and power

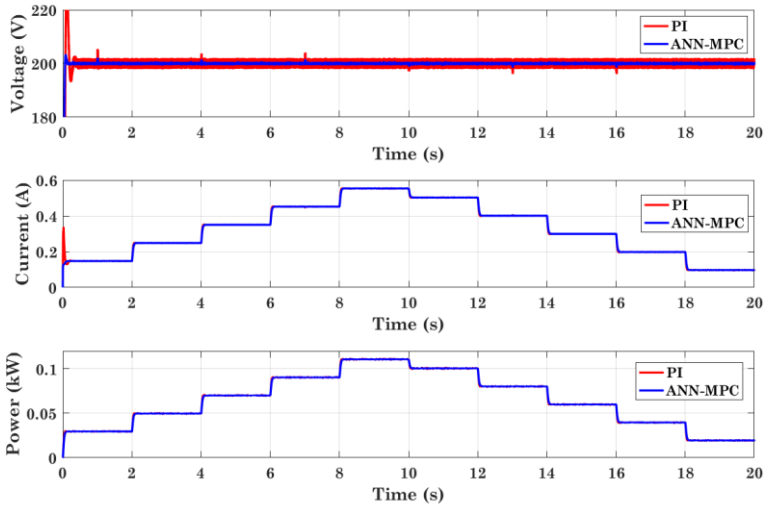

(a)

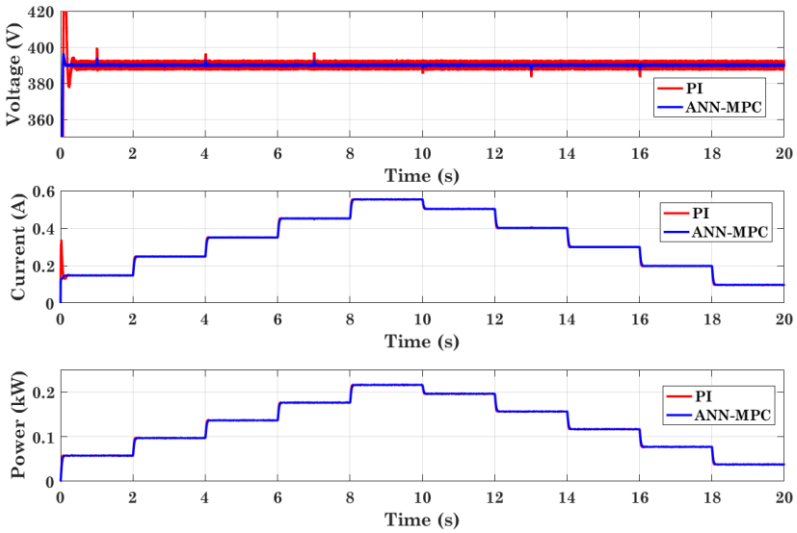

(b)

Figure 18. Electrolyzer Voltage and current (a) Electrolyzer voltage, current and power (b) Electrolyzer converter input voltage, current and power

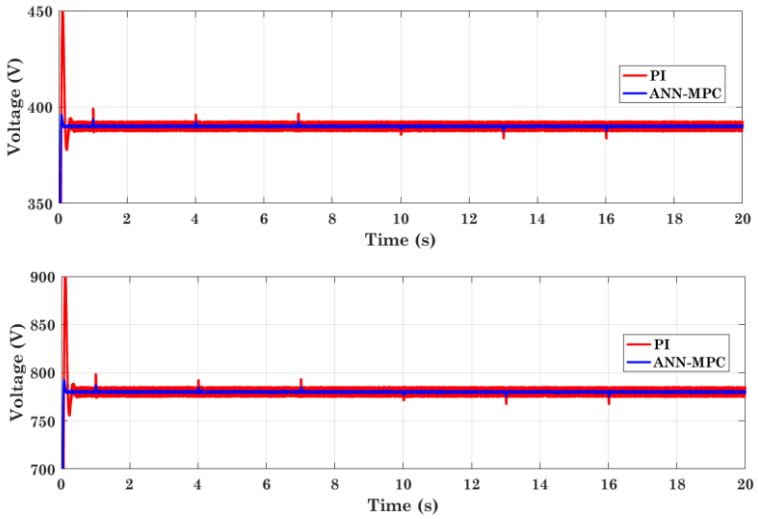

Figure 19. QBBC input voltage and output voltage

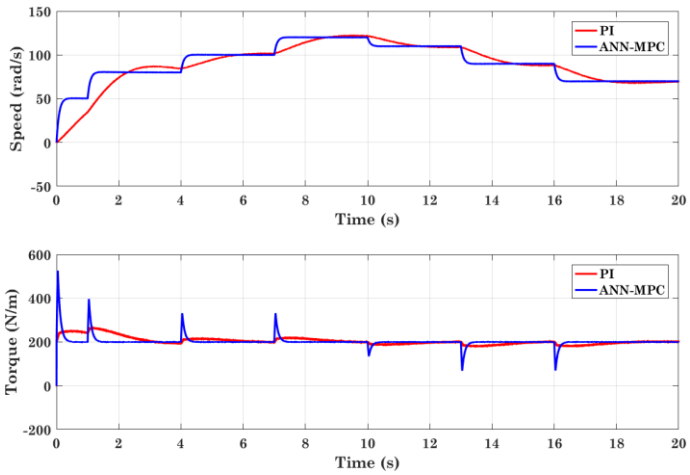

Figure 20. Motor Speed and Torque (a) with PI Control (b) with Proposed Control

CASE3: In this scenario, the vehicle suddenly accelerates from 100 rad/s to 150 rad/s at the 10-seconds. The load torque undergoes several fluctuations: it increases from 40 Nm to 90 Nm at 2.5 seconds, further rises to 210 Nm at the 5th second, then decreases to 170 Nm at 7.5 seconds, and subsequently to 140 Nm at the 10th second. The load torque then steadily declines to 110 Nm at the 12.5-second, further drops to 60 Nm at the 15th second, and ultimately reaches 40 Nm at the 17.5-second. Figure 21(a) illustrates the speed and torque of the vehicle drive, capturing these dynamic changes. Figure 21(b) provides a detailed insight into the voltage, current, and power output from the solar panel. Figure 22(a) presents similar information for the fuel cell, demonstrating its performance under varying workloads. Furthermore, Figure 22(b) depicts the active and reactive power of the motor, offering insights into its behavior during the simulation. These results offer a comprehensive understanding of how the EV system responds to changes in speed and load torque, showcasing its adaptability and performance under dynamic operating conditions.

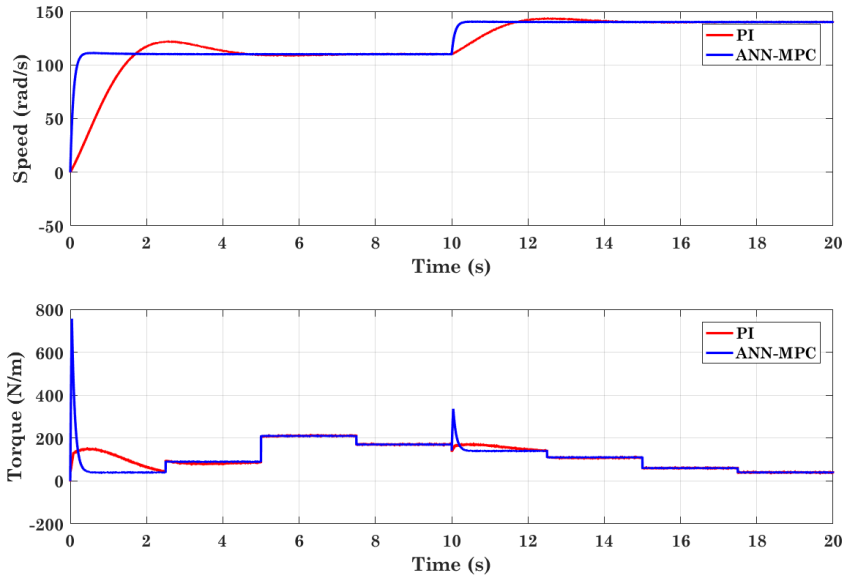

(a)

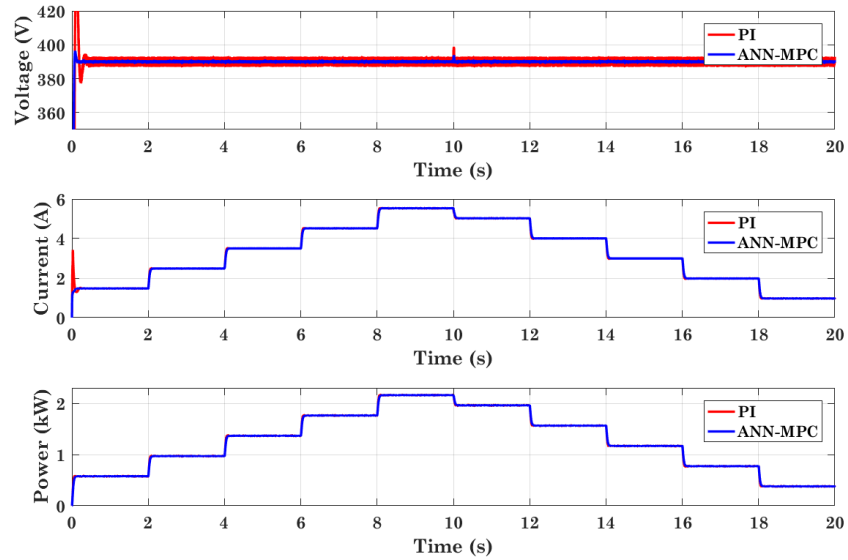

(b)

Figure 21. (a) Motor Speed and Torque. (b) PV converter output voltage, current and power

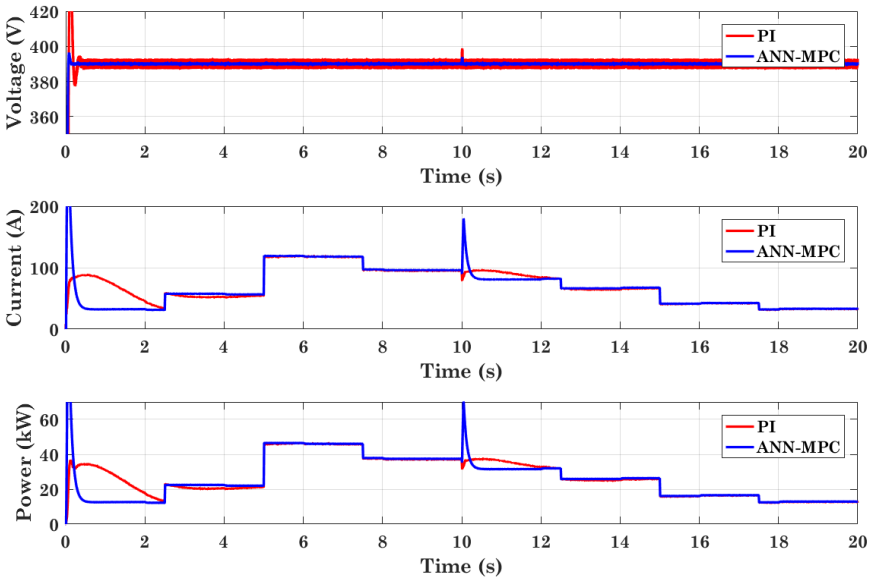

(a)

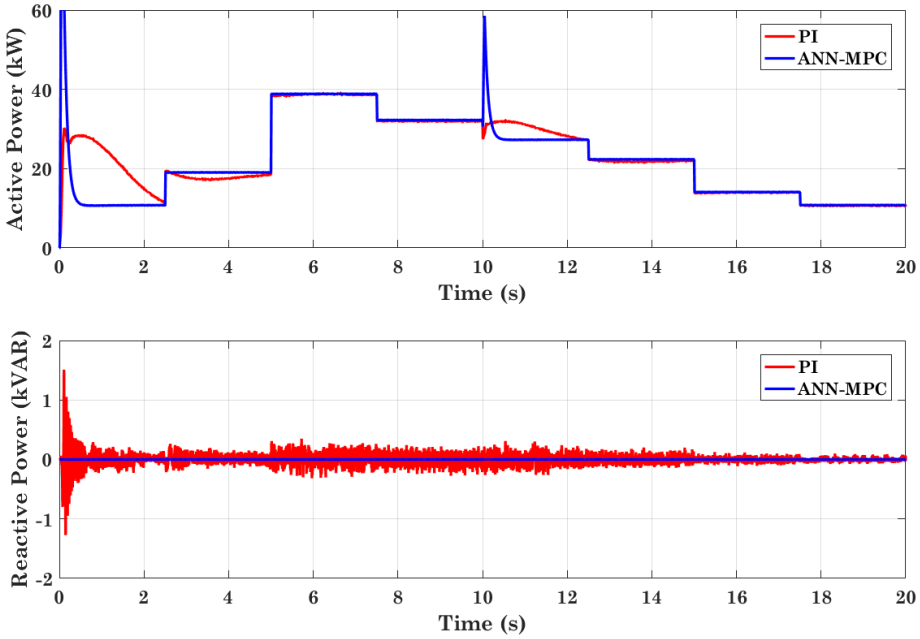

(b)

Figure 22. (a) FC converter output voltage, current and power, (b) Motor Input active and reactive power

VI. CONCLUSION

The integration of advanced MPC based on ANN technology within the HEV setup offers promising avenues for enhancing efficiency and performance. This study underscores the successful incorporation of crucial components like the Photovoltaic (PV) array, fuel cell, and electrolyzer, elucidating their roles in bolstering the vehicle's power supply system. Through comprehensive simulation studies, the performance and efficiency of the proposed EV configuration under varying irradiance and speed conditions are meticulously evaluated, demonstrating its adaptability and effectiveness. The utilization of Maximum Power Point Tracking (MPPT) algorithms and refined control strategies for voltage regulation contributes to optimizing the PV system's efficiency and economic feasibility. Furthermore, the deployment of ANN-based MPC for motor speed regulation showcases superior control accuracy compared to traditional control methods like Proportional-Integral (PI) controllers. The

introduction of a novel approach for torque control of AC machines using ANN estimators represents a significant advancement in control techniques, eliminating the need for weighting factors. Comparative analysis with conventional control methods serves to validate the efficacy of the proposed techniques and strategies. Overall, the research presented in this paper contributes to the ongoing evolution of efficient and intelligent electric vehicle systems capable of integrating renewable energy sources and optimizing energy management. It lays a solid groundwork for further exploration and advancement in this domain, aiming to address the challenges of sustainability and environmental impact in the transportation sector.

REFERENCES

[1] Dluhopolskyi, Oleksandr, Serhii Kozlovskyi, Yurii Popovskyi, Svitlana Lutkovska, Vira Butenko, Taras Popovskyi, Hennadii Mazur, and Andrii Kozlovskyi. "Formation of the model of sustainable economic development of renewable energy." ECONOMICS-Innovative and Economics Research Journal 11, no. 2 (2023): 51-78.

[2] He, Yingdong, Yuekuan Zhou, Zhe Wang, Jia Liu, Zhengxuan Liu, and Guoqiang Zhang. "Quantification on fuel cell degradation and techno-economic analysis of a hydrogen-based grid-interactive residential energy sharing network with fuel-cell-powered vehicles." Applied Energy 303 (2021): 117444.

[3] Huang, Qirong. "Analysis of Global Policy and Impact on Automobile Industry under Carbon Neutrality." In E3S Web of Conferences, vol. 308, p. 01021. EDP Sciences, 2021.

[4] Kim, S., Tanim, T.R., Dufek, E.J., Scoffield, D., Pennington, T.D., Gering, K.L., Colclasure, A.M., Mai, W., Meintz, A. and Bennett, J., 2022. Projecting recent advancements in battery technology to next-generation electric vehicles. Energy Technology, 10(8), p.2200303.

[5] Afshar, Shahab, Pablo Macedo, Farog Mohamed, and Vahid Disfani. "Mobile charging stations for electric vehicles—A review." Renewable and Sustainable Energy Reviews 152 (2021): 111654.

[6] Lakshmi, G. Sree, S. Kamakshaiah, and Tulasi Ram Das. "Closed loop PI control of PMSM for hybrid electric vehicle using three level diode clamped inverter for optimal efficiency." In 2013 International Conference on Energy Efficient Technologies for Sustainability, pp. 754-759. IEEE, 2013.

[7] Eltoumi, Fouad M., Mohamed Becherif, Abdesslem Djerdir, and Haitham S. Ramadan. "The key issues of electric vehicle charging via hybrid power sources: Techno-economic viability, analysis, and recommendations." Renewable and Sustainable Energy Reviews 138 (2021): 110534.

[8] Buresh, Kevin. "Impacts of electric vehicle charging in South Africa and photovoltaic carports as a mitigation technique." PhD diss., Stellenbosch: Stellenbosch University, 2021.

[9] Inci, Mustafa, Murat Mustafa Savrun, and Özgür Çelik. "Integrating electric vehicles as virtual power plants: A comprehensive review on vehicle-to-grid (V2G) concepts, interface topologies, marketing and future prospects." Journal of Energy Storage 55 (2022): 105579.

[10] Dada, Modupeola, and Patricia Popoola. "Recent advances in solar photovoltaic materials and systems for energy storage applications: a review." Beni-Suef University Journal of Basic and Applied Sciences 12, no. 1 (2023): 1-15.

[11] Mauler, L., Duffner, F., Zeier, W. G., & Leker, J. (2021). Battery cost forecasting: a review of methods and results with an outlook to 2050. Energy & Environmental Science, 14(9), 4712-4739.

[12] Yang, M., Zhang, L., Zhao, Z., & Wang, L. (2021). Comprehensive benefits analysis of electric vehicle charging station integrated photovoltaic and energy storage. Journal of Cleaner Production, 302, 126967.

[13] Heo, J., Jung, J., Kim, B., & Han, S. (2020). Digital elevation model-based convolutional neural network modeling for searching of high solar energy regions. Applied energy, 262, 114588.

[14] Hachem-Vermette, Caroline. Solar Buildings and Neighborhoods: Design Considerations for High Energy Performance. Springer Nature, 2020.

[15] Latha, K. Sree, and M. Lakshmi Swarupa. "Design and implementation of power conditioning for distribution network V2G to electric vehicle and DC charging system." In AIP Conference Proceedings, vol. 2269, no. 1. AIP Publishing, 2020.

[16] Wang, Yuhang, and Jingbo Fan. "Technological Mediation of Photovoltaic System to Improve Rural Sustainability in the Background of Resettlement and Consolidation: Evidence from the Rural Community and Villages in China." Sustainability 15, no. 12 (2023): 9579.

[17] Cieslik, Wojciech, Filip Szwajca, Wojciech Golimowski, and Andrew Berger. "Experimental analysis of residential photovoltaic (PV) and electric vehicle (EV) systems in terms of annual energy utilization." Energies 14, no. 4 (2021): 1085.

[18] Yan, M., Xu, H., Jin, L., He, H., Li, M. and Liu, H., 2022. Co-optimization for fuel cell buses integrated with power system and air conditioning via multi-dimensional prediction of driving conditions. Energy Conversion and Management, 271, p.116339.

[19] Jafari Kaleybar, Hamed, Hossein Hafezi, Morris Brenna, and Roberto Sebastiano Faranda. "Smart AC-DC Coupled Hybrid Railway Microgrids Integrated with Renewable Energy Sources: Current and Next Generation Architectures." Energies 17, no. 5 (2024): 1179.

[20] Divya, G, Venkata Padmavathi S. "Design and Modeling of Hybrid Electric Vehicle Powered by Solar and Fuel Cell Energy with Quadratic Buck/Boost Converter." WSEAS Transactions on Circuits and Systems 22 (2023): 41-54.